Surface Mechanical Attrition Treatment of Additively Manufactured 316L Stainless Steel Yields Gradient Nanostructure with Superior Strength and Ductility

Sumit Ghosh[a,#], Nitish Bibhanshu[a], Satyam Suwas[a], Kaushik Chatterjee[a]*

[a] Department of Materials Engineering, Indian Institute of Science, Bangalore-560012, Karnataka, India.

[#]Current address:

Materials and Mechanical Engineering, Centre for Advanced Steels Research, University of Oulu, 90014 Oulun yliopisto, Finland.

*Corresponding author:

Email: kchatterjee@iisc.ac.in

Phone: +91-80-2293-3408

Fax: +91-80-2360-0472

Abstract

Surface severe plastic deformation (S^2PD) of additively manufactured/ three-dimensional (3D) printed metallic parts is gaining increased attention as a post-manufacturing operation to enhance the material performance in a wide variety of applications. Surface mechanical attrition treatment (SMAT) is an S^2PD technique that can yield a nanostructured surface layer induced by compressive stresses and work hardening. In the present study, SMAT was performed on 316L (austenitic) stainless steel (SS) processed by selective laser melting (SLM), and the consequent effects on mechanical response were investigated. The underlying mechanisms of microstructural evolution leading to the formation of nanocrystalline grains resulting from SMAT in SLM 316L SS are elucidated. The interactions between twins and deformation bands act as potential sites for impeding the movement of dislocations, which in turn leads to the formation of stacking faults, twinning, and occasionally transform to a different crystal structure. Twin-twin and/or twin-deformation band intersections sub-divide the matrix grains into smaller cells or low-angle disoriented blocks, which result in the formation of low-angle grain boundaries and finally in nanocrystallization at the surface. The size of nanocrystalline grains increases progressively with depth from the surface to micrometer size grains in bulk. The gradient nanostructure in the additively manufactured alloy after SMAT imparts an unusual combination of strength and ductility that markedly exceeds that of conventional, bulk nanostructured, or even high-performance 316L SS (containing nanoscale deformation twins embedded in submicron-sized austenitic grains obtained by dynamic plastic deformation processes). Analytical models revealed that strengthening results from a combination of grain boundaries and dislocations. The results of the present investigation pave the way for engineering high-performance SS for a variety of engineering applications.

1. Introduction

Additive manufacturing (AM) offers unprecedented potential for manufacturing end-to-end customized products in several domains such as automobile, aerospace and biomedical devices [1-4]. However, building customized products with high performance by AM presents a technological challenge and requires continued research [1-4]. Among the different AM processes, selective laser melting (SLM) has emerged as one of the most preferred AM processing routes for the fabrication of near-net-shaped metallic components with complex geometries and high dimensional accuracy [1,2]. Metal parts prepared by AM suffer from characteristic limitations such as residual tensile stresses, undesired microstructure, voids, and poor surface finish, etc., that compromise their mechanical performance compared to the parts prepared by conventional subtractive manufacturing.

Surface engineering strategies to improve the performance of the additively manufactured parts are widely investigated. Surface mechanical attrition treatment (SMAT) is an efficient, eco-friendly, and cost-effective surface severe plastic deformation (S^2PD) technique that generates a gradient nanostructured layer on the surface by inducing compressive stresses and work hardening. [5-7]. SMAT is essentially a variation of the conventional shot peening process. The balls impact the surface at well-defined incidence angles in shot peening, whereas, in SMAT the impacts are in more random directions [6,7]. In this process, small particles repetitively impact a material surface using an ultrasonic transducer. SMAT provides more precise control on the working parameters and is suitable for treating complex structures. It has been reported that SMAT leads to a gradient nanostructure from the surface into the bulk of the materials, and this can concurrently improve the performance such as fatigue life, wear resistance, corrosion resistance, and interestingly, even the biological response to the materials [6-10].

Mechanisms underlying nanocrystallization resulting from SMAT have been investigated for conventionally processed 304 and 316L stainless steels [11-13]. Zhang et al. [11] reported the formation of surface nanocrystals after SMAT of 304 stainless steel (SS) obtained by rolling and annealing (average grain size 100 to 200 μm), and the mechanism therein was identified as grain sub-division due to extensive formation of twins followed by twin-twin intersections. On the other hand, Thangaraj et al. [12] reported strain-induced martensitic transformation of austenite after SMAT of 304 SS (average grain size 40 to 50 μm). Such a transformation was, however,

not observed in 316L SS (average grain size of 35 μm) [13], which was attributed to the stability of the austenite phase in 316 L SS owing to higher nickel content.

The deformation behavior of FCC metals and alloys is known to depend on the stacking fault energy (SFE). Studies carried out on a range of Ni-xCo alloys [14-16] have revealed that for an alloy with intermediate SFE (Ni-40Co), the deformation mechanism is primarily mediated by slip followed by shear banding, while in the low SFE alloy (Ni-60Co), the deformation mode changes from slip to twin early stages itself followed by shear banding. For high strain rate deformation, the formation of fine twins has been reported [17] even in the early stages of deformation. A microstructure with a high density of twins not only promotes the subdivision of grains but also leads to significant strengthening [7,18]. The formation of strain-induced martensite followed by twinning has been reported for low SFE SSs, while in the case of SS with relatively higher SFE, only dislocation cells and tangles form with the progress of deformation [19,20]. A recent study [21] has reported the formation of nanocrystals after SMAT of wrought 316L SS, and the same has been attributed to dynamic recrystallization in shear bands rather than twinning. The propensity of twinning depends on the total strain and strain rates (frequency in the case of SMAT) [11-15]. The results from a number of investigations have indicated grain size as an important factor, and it has been shown that, at least in the microcrystalline range, a reduction in grain size typically makes twinning more difficult [22-25]. Zhu et al. [26,27] carried out a systematic study to understand the role of grain size on deformation twinning and detwinning in FCC metals for a wide range of grain sizes encompassing micro- to nanocrystalline regimes. They reported that with a decrease in grain size, deformation by twinning is more difficult in the coarse grain regime. In contrast, nanocrystalline FCC metals first become amenable for deformation by twinning.

Although the nanocrystallization by S^{2}PD techniques in different conventionally processed wrought alloys is well documented [7, 11-13, 18-21], the information available on the effect of S^{2}PD of additively manufactured alloys is rather scarce. Since the additively manufactured alloys exhibit characteristic microstructures consisting of fine cellular features, melt pool boundaries, etc., that are remarkably different from wrought materials, it is highly desirable to investigate the evolution of micro-/nano-structures in these alloys after S^{2}PD. There are no reports on the mechanism of nanocrystallization or underlying strengthening mechanisms

for 316L SS prepared by AM subjected to S^{2}PD. Furthermore, fine cellular microstructure within melt pool boundary in SLM processed AM materials consists of a complex network of dislocations with the segregation of alloying elements (Mn, Cr, Ni, etc.) at the cell boundaries due to cellular growth mode under high-temperature gradient and high growth rate conditions [28]. The complex network of dislocations with a segregated interface significantly tunes the dislocation behavior during deformation. The dislocation network boundaries act as a filter to slow down the dislocation motion during plastic deformation [28]. Hence, the mechanism of nanocrystallization by SMAT in the case of additively manufactured 316L SS is envisaged to differ from that compared to SMAT on wrought materials.

In view of the above, the present investigation has been aimed at developing a comprehensive understanding of the deformation behavior and mechanism of nanocrystallization through a detailed investigation of microstructural features. The evaluation of consequent mechanical properties in 316L SS prepared by SLM and subjected to SMAT has been carried out. Since dislocation slip and deformation twinning are competitive mechanisms, the relative influence of these two mechanisms on the microstructural evolution is vital for developing nanocrystalline and/or nanotwinned surface-hardened additively manufactured materials. Furthermore, in view of the influence of accumulated compressive stresses on the tensile behavior, a systematic investigation has been carried out to unravel the role of gradient structure formed by SMAT on the mechanical properties of AM 316L SS. Microstructural features have been examined using electron back-scattered diffraction (EBSD) and transmission electron microscopy (TEM) techniques, as well as the bulk estimation of dislocation density and crystallite size by X-ray line profile analysis. Finally, the contribution of individual strengthening mechanisms has been estimated using analytical models to corroborate the enhancement of yield strength through SMAT.

2. Materials and methods

2.1. Processing methodology

AM samples of 316L SS were obtained from INTECH DMLS Pvt. Ltd, Bangalore, India. These samples were prepared by SLM (EO SINT M 280) using a 195 W power laser with a scanning speed of 650 mm/s. The average particle size of the powder was 35 μm. The last layer was printed using different parameters in order to obtain a superior surface finish as a standard

protocol by the company. The scanning direction and strategy used are presented schematically in Fig. 1a. A bidirectional scanning strategy was used, wherein the next layer was deposited in the same manner at 67° rotation with respect to the underlying layer, as shown in Fig. 1a. Rectangular cuboids (dimension $7 \times 7 \times 1$ mm^3) and dog-bone-shaped samples (gage length of 6 mm, gage width 2 mm, and thickness 1 mm) were prepared in horizontal build orientation (Fig. 1a).

Prior to subjecting to SMAT, all the samples were mechanically polished up to 3000 grit emery paper followed by electropolishing. SMAT was conducted at a frequency of 30 Hz with 4.75 mm hardened steel balls of hardness 50 HRC for a duration of 15 to 60 min. The SMAT unit used in the present investigation was fabricated by Cosmic Industrial Laboratories Limited, Bengaluru, India, and consists of a cylindrical chamber of 170 mm diameter [29]. A total of 500 balls were used. The distance between the specimen surface and the base of the chamber was fixed at 20 mm.

2.2. Microstructural characterization

As-AM and SMAT-processed specimens were mechanically polished using different grades of emery papers followed by etching prior to an investigation by optical microscopy (Zeiss) and scanning electron microscopy (SEM, Sirion, FEI). Electron back-scattered diffraction (EBSD, Helios NanoLab Dual Beam, FEI) scans were performed with a step size of 50 nm to analyze the cross-section. Samples for EBSD analysis were prepared by slandered mechanical polishing followed by electropolishing (Struers Lectropol 5) at 28 V in an electrolyte of the following composition: 100 ml butoxy ethanol, 78 ml perchloric acid, 730 ml ethanol, and 70 ml distilled water. To prepare sample for transmission electron microscopy (TEM, FEI Tecnai F-30), the cross-sectional lamella was sectioned out at a depth of a few micrometers from the surface by focused ion beam milling using Gallium ions at 30 kV, followed by lower-current thinning.

2.3. Mechanical characterization

Mechanical properties were evaluated from tensile tests performed at a constant strain rate 10^{-3} s^{-1} on a universal testing machine (Instron 5967). Specimens for tensile tests were prepared following ASTM: E8 standards. Vickers microhardness (Future-Tech FM-800) measurements

were performed at a load of 10 gf and a dwell time 10 s along the cross-section at various depths from the surface.

2.4. X-ray diffraction and estimation of microstructural parameters

X-ray diffraction (XRD) measurements were performed using Cu-Kα radiation (Rigaku Smart Labs) in the 2θ range 35° to 100° at 30 mA current and 45 kV voltage with a step size 0.02 and a scan speed of 0.1° min^{-1}. The estimation of dislocation density and crystallite size was carried out using Williamson-Hall Analysis [43,44].

3. Results and Discussion

3.1. Microstructural features revealed by optical and scanning electron microscopy

The microstructure of the as-AM material was characterized on X-Y and X-Z planes where Z is taken as the build direction, as shown schematically in Fig. 1a. Fig. 1b represents the optical micrograph on the X-Y plane, (as marked in Fig. 1a), which exhibits elongated melt pools revealing the laser scanning path. The melt pools are seen to be oriented in two different directions at an angle of 67°, which is the rotation angle of scanning between successive printed layers, as described above. Each layer comprising of overlapping domains has a width of ≈100 µm. Such characteristic features have been reported earlier for 316L SS prepared by SLM [30].

The scanning electron micrograph on the X-Z plane (Fig. 1c) reveals the cellular microstructure (≈34 ± 12 µm) in the as-AM material. The cells formed after solidification have polygonal cross-sections (Fig. 1c). Melt pool boundaries (Fig. 1d) formed in the successive layer are also observed in the SEM micrograph, corroborating reported findings [2-4]. These melt pool boundaries are formed due to the non-equilibrium heating/cooling cycles experienced during SLM. The melt pool boundaries appear brighter than the cells indicating possible enrichment by heavier elements such as Cr, Mo, and Ni, etc. [2-4].
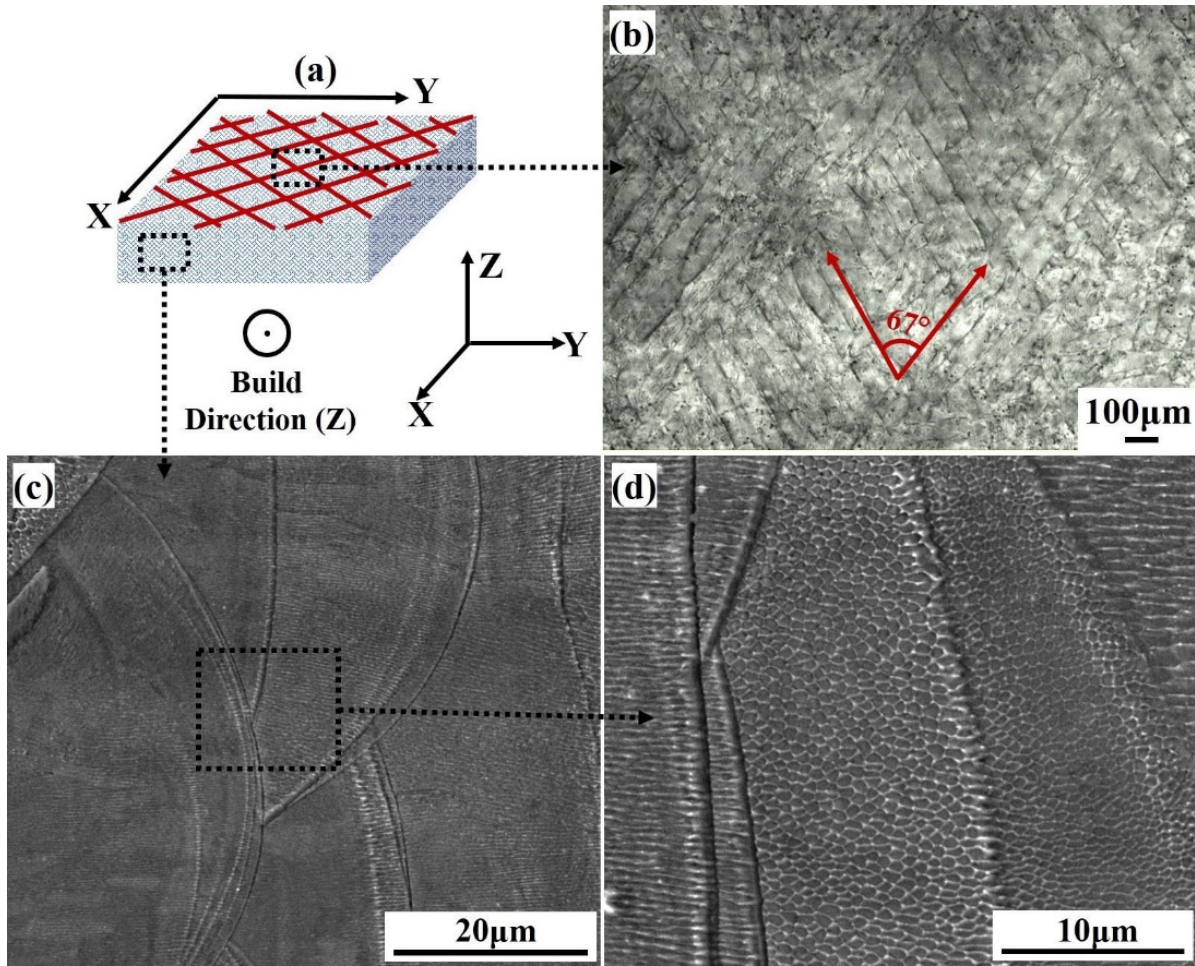
Fig. 1: (a) Schematic representation of horizontally built sample, (b) Optical micrographs of the top surface of the horizontally built sample, (c, d) cross-sectional views under SEM at a different section of the horizontally built sample.

EBSD generated IPF map, as well as the corresponding KAM map of as-AM, are presented in Figs. 2a and 2b. The IPF map essentially reveals epitaxial grains, whereas the KAM map shows uniform distribution of strain throughout the matrix without the presence of any strain gradient.
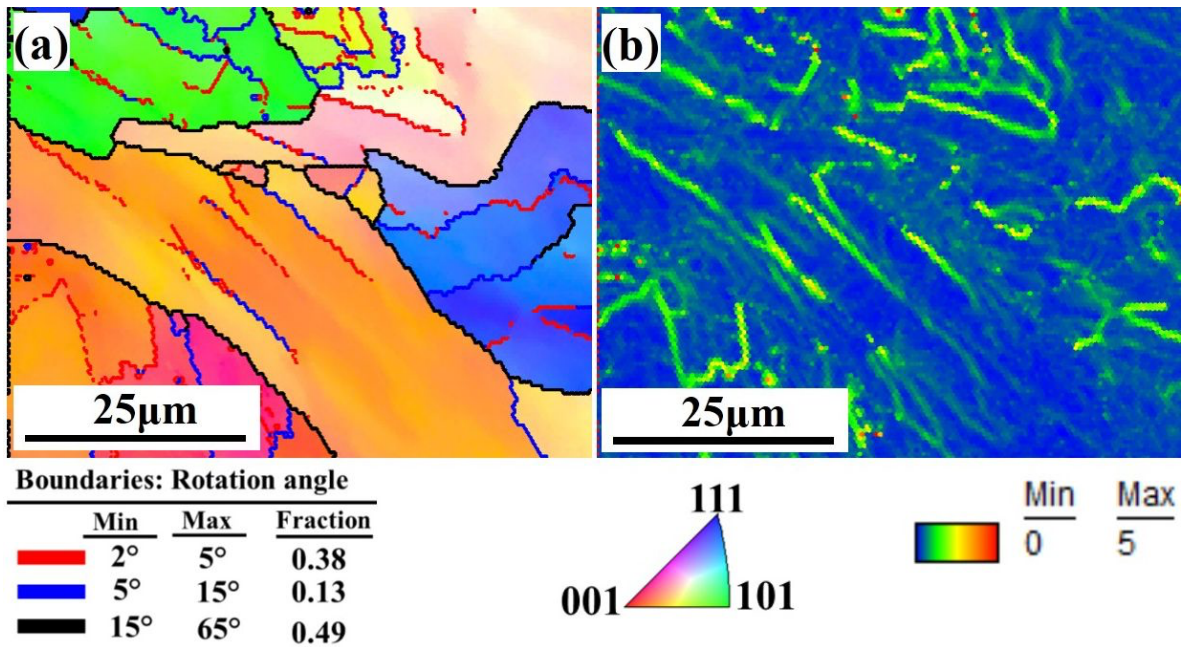
Fig. 2: (a) EBSD inverse pole figure (IPF) map superimposed with grain boundary (GB) map of additively manufactured materials, and (b) the corresponding kernel average misorientation (KAM) map.

Figs. 3a and 3b present the micrographs of the sample cross-section after subjecting to SMAT for 15 and 60 min, respectively. Hereafter, the samples are referred to as SMAT-15 and SMAT-60. A high density of etch pits is observed at depths of ≈20 to 25 μm and ≈30 to 35 μm from the treated surfaces for SMAT-15 and SMAT-60, respectively (Figs. 3a and 3b). The depth of these etch pits is not the same at the two depth levels. Due to SMAT, defect generation at the surface can be regarded as preferential pit initiation sites on etching. It is to be noted that prolonged SMAT has led to an increase in the thickness of the affected zone, as revealed by the thicker gradient layer in SMAT-60 compared to SMAT-15.
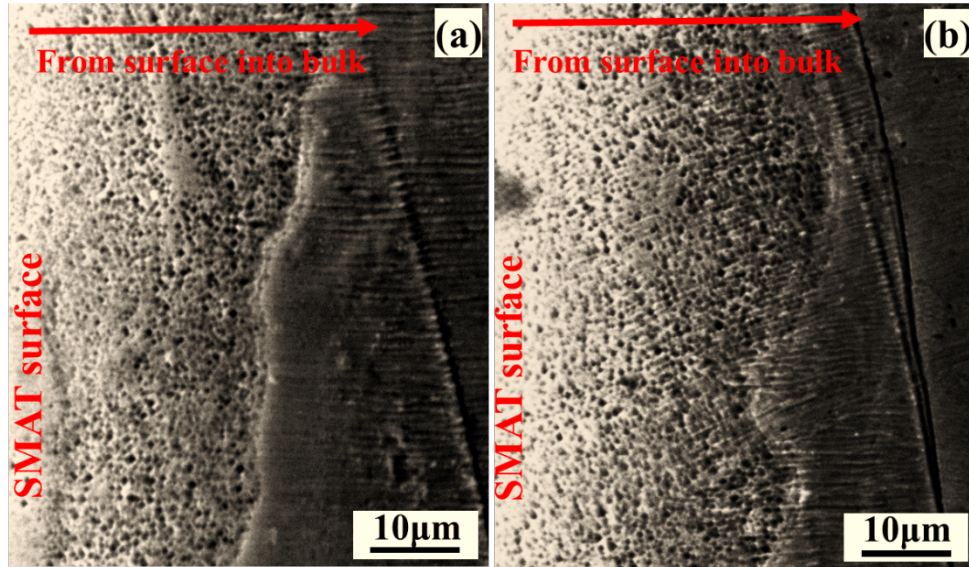
Fig. 3: Cross-sectional view of (a) SMAT-15 and (b) SMAT-60 samples under SEM.

SMAT-induced plastic deformation resulted in significant refinement of the grains at the surface. Generally, dislocation activity and deformation twinning have been considered as the principal deformation modes in severe plastic deformation (SPD) of metals [31-34]. Dislocation tangles and specific subgrain structures such as dislocation cells, walls, geometrically necessary boundaries, and incidental dislocation boundaries are generated, which ultimately lead to grain refinement when metallic material is subjected to SPD [31-34].

3.2. Gradient microstructure after SMAT

Cross-sectional EBSD scans of additively manufactured material before and after SMAT were measured at ≈50 µm depth from the surface. Fig. 4a presents the inverse pole figure (IPF) map superimposed with the grain boundary (GB) map of SMAT-15. The EBSD scan could not be indexed in the region adjacent to the surface due to the large accumulated strain. The dark zone in the image represents heavily strained regions giving rise to overlapped Kikuchi patterns, and hence, could not be indexed. Bahl et al. [21] and Samih et al. [35] reported similar EBSD maps for wrought 316L SS after SMAT. As shown in Fig. 4a, EBSD could not resolve the structure up to ≈4 µm below the surface. This region consists of the heavily deformed microstructure, including nanocrystalline grains along with high dislocation density (in the other regions) or other microstructural features smaller than 50 nm [21,35]. As the distance from the surface increases, EBSD scans reveal fine domains that represent grains and subgrains. At ≈15 µm below

the surface, a subdivision of the original grains into smaller blocks/ domains can be seen. Most of these domains exhibit a high fraction of low angle boundaries. Figs. 4b and 4c present the magnified image of the corresponding IPF map, as marked in Fig. 4a. The subdivision of matrix grains by low-angle grain boundaries is seen in Figs. 4b and 4c.
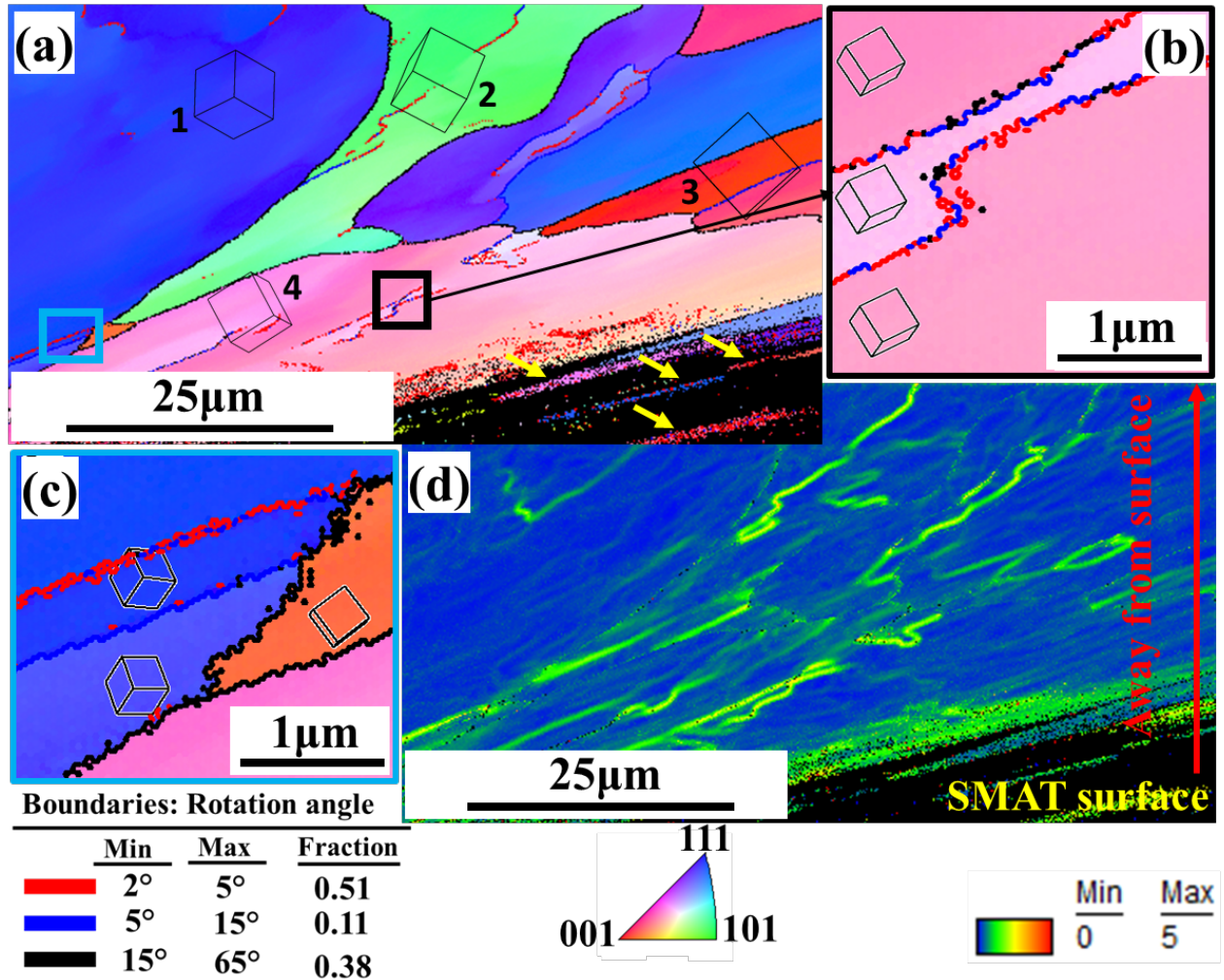

Fig. 4: (a) EBSD inverse pole figure (IPF) map superimposed with grain boundary (GB) map of SMAT-15, (b, c) magnified image of the marked regions of the IPF map in (a), and (d) kernel average misorientation map (KAM) of the region corresponding to (a). The dark regions in (a) indicated by yellow arrows indicate the highly deformed regions near the surface.

Fig. 4d represents the kernel average misorientation (KAM) map of the corresponding specimen. Higher KAM value adjacent to the surface compared to the bulk sample further corroborates that SMAT-induced plastic deformation at the surface. The strain distribution

profile from the surface into the bulk reveals that extensive strain is generated adjacent to the surface due to SMAT and the strain gradually decreases with increasing depth. Thus, the accumulated compressive strained layer is essentially up to ≈20 μm depth.
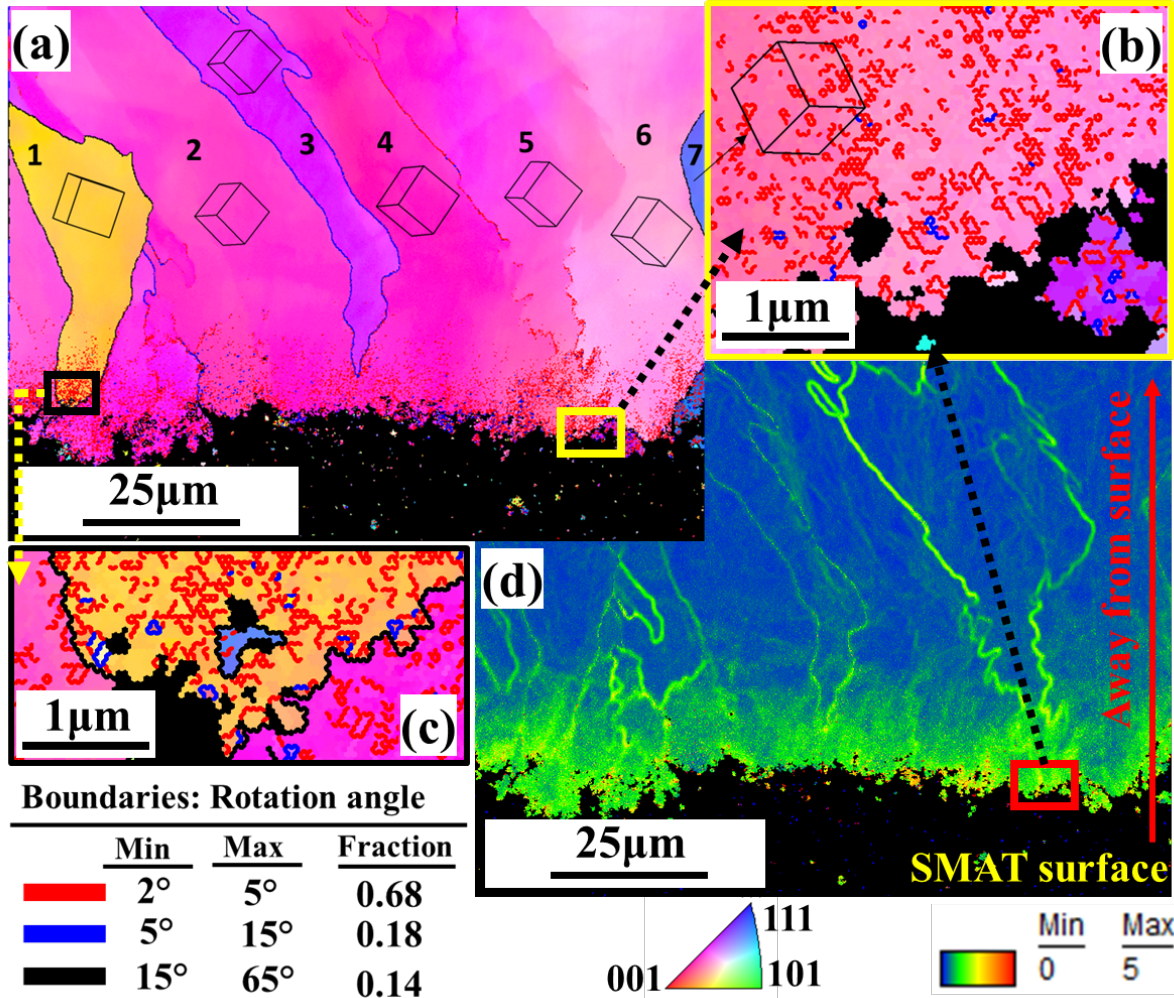

Fig. 5: (a) EBSD inverse pole figure (IPF) map superimposed with grain boundary (GB) map of SMAT-60, (b, c) magnified images of the marked regions in the IPF map as indicated in (a), (d) kernel average misorientation map (KAM) of the region corresponding to (a).

Fig. 5a presents the IPF map superimposed with GB map for SMAT-60. A larger section of the image could not be indexed (as compared to SMAT-15), likely due to the larger strain accumulation than in SMAT-15. At a distance of ≈25 μm from the surface, a large fraction of subgrains with a high fraction of low-angle boundaries can be observed. Figs. 5b and 5c present

magnified images of the corresponding regions of the IPF map indicated in Fig. 5a. Fragmentation of the initial matrix grains by low-angle grain boundaries is observed that resulted from heavy deformation. The KAM map in Fig. 5d reveals strain gradients adjacent to the surface similar to those observed in SMAT-15, which gradually decrease with increasing depth. In this case, the depth of the compressively strained layer is ≈35 μm. Thus, the duration of SMAT strongly influences the thickness of the gradient layer.
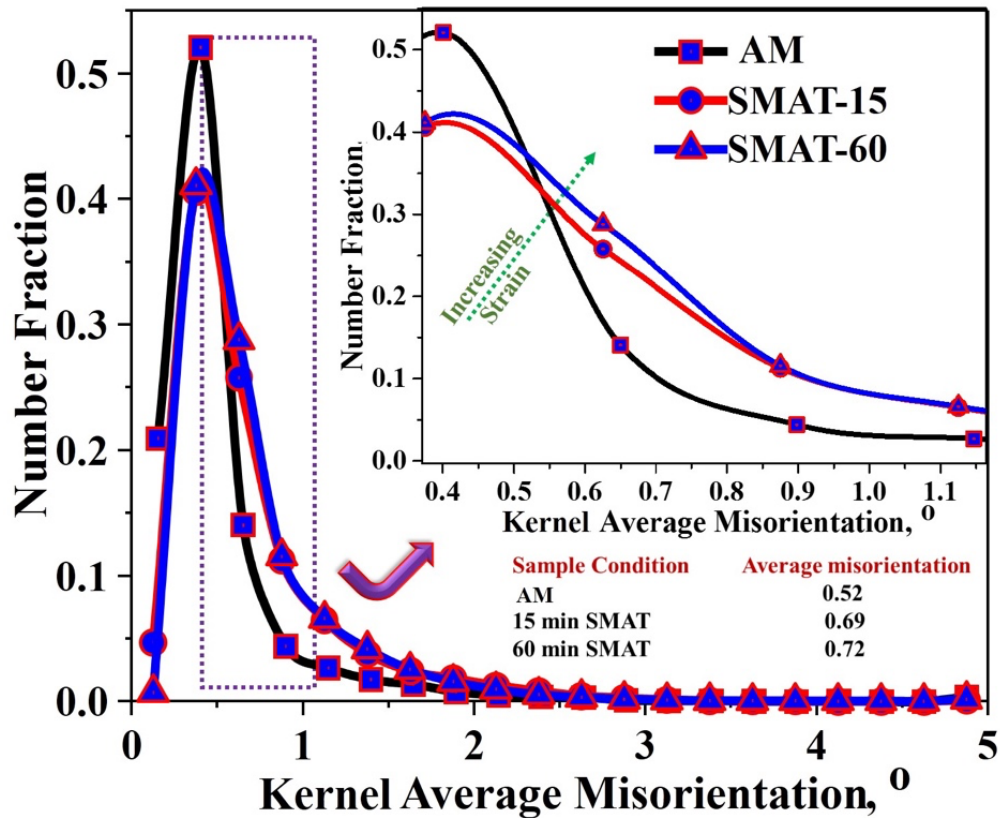

Fig. 6. Average KAM values of additively manufactured, SMAT-15 and SMAT-60 materials. Inset presents the data corresponding to the dotted region for enhanced clarity.

Fig. 6 compiles the average quantified KAM values of all the samples. The average KAM value of the AM sample is ≈0.52, which increased to 0.69 and 0.72 for SMAT-15 and SMAT-60, respectively. These results are in good agreement with the hardness measurements described below.

13

3.3. Nanostructural features revealed by transmission electron microscopy

TEM was used to reveal nanoscale features formed due to SMAT. Thin lamellae were prepared by FIB milling to reveal the features at various locations from the surface into the bulk. The plane-view TEM foils of the layers at different depths are shown in Fig. 7.
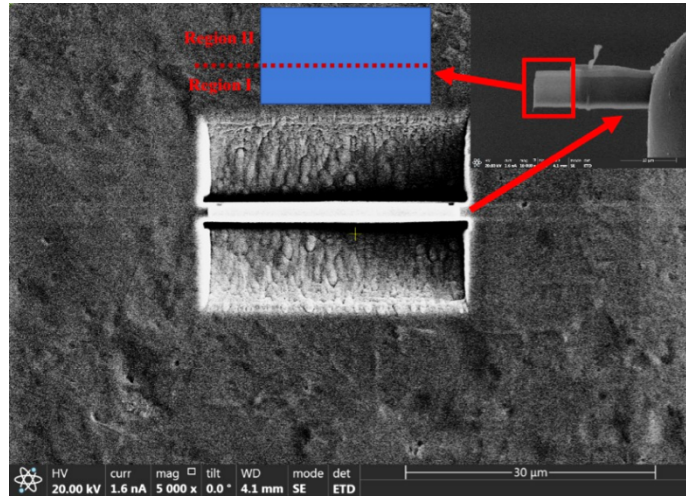

Fig. 7: Extraction of thin lamella from SMAT cross section using focused ion beam milling (FIB).
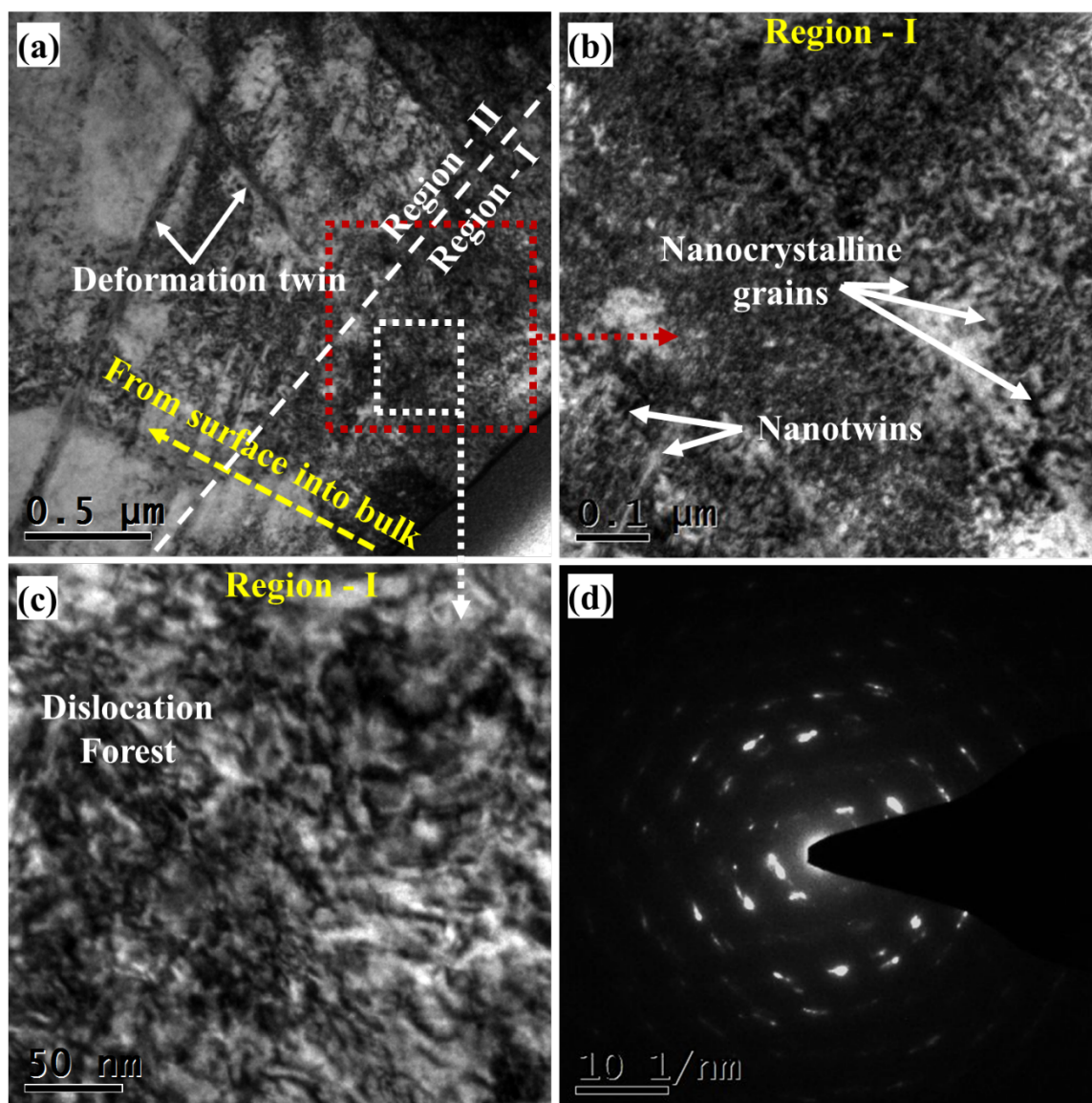
Fig. 8: (a) Bright-field TEM micrograph of the region adjacent to the top surface layer, (b) Magnified view of selected location as marked in (a). Inset shows the diffraction pattern from the top surface layer

Fig. 8a shows the bright-field TEM micrograph of the sample SMAT-60. The micrograph in Fig. 8a can be visualized as a combination of two regions- I and II depending on the distance from the surface toward the bulk. Figs. 8b and 8c show higher magnification micrographs of the selected region in Fig. 8a. It can be noticed in Fig. 8b that SMAT led to nanocrystallization at the surface resulting in average grain size ≈ 50 nm. Fig. 8c reveals the presence of a dense dislocation forest in the SMAT-affected zone up to 2 μm from the surface, which is a

characteristic of materials subjected to large plastic deformation [8]. The selected area diffraction pattern (SADP) shown in Fig. 8d further confirms the formation of highly refined nanostructured grains adjacent to the surface. It was observed that the density of dislocation gradually decreases with increasing distance from the surface. Thus, SMAT induces a strain gradient from the surface to the bulk along with a gradient in grain size. In region-I, the material underwent the most intense plastic deformation, and therefore, exhibits high dislocation density that reduces the mobility of dislocations in this region. In such a case, stacking faults and twins tend to form, as shown in Figs. 9(a, b c). The diffraction pattern presented in Fig. 9c was recorded from the region marked Fig. 9b and represents a stacking fault. The diffraction pattern indicates the existence of two phases, the original austenitic phase and another structure revealed by the faint spots. The double diffraction in the fainted spots corresponds to twins formed during the deformation.
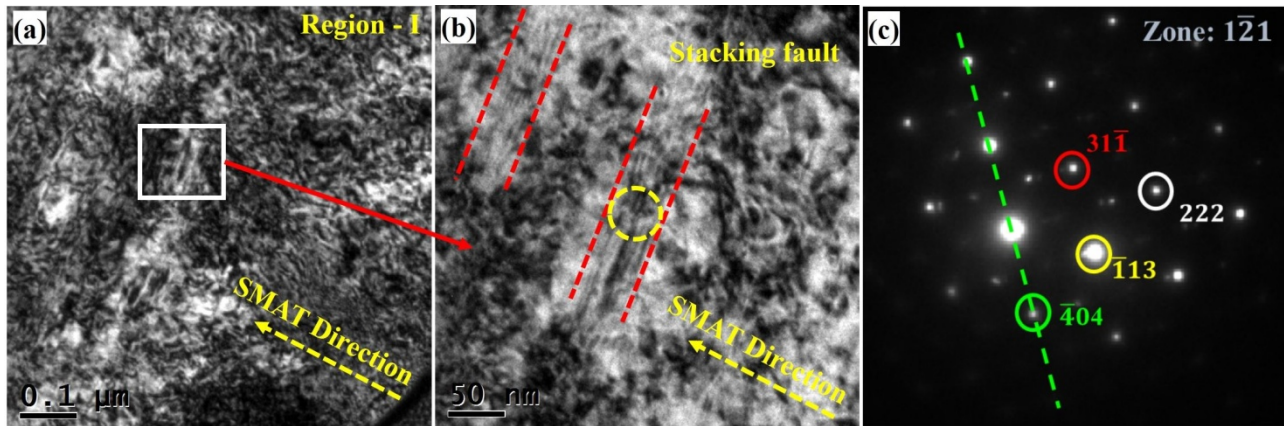

Fig. 9: (a) Bright-field TEM micrograph of the region adjacent to the top surface layer, (b) magnified view of selected location as indicated in Fig 9a, (c) SADP from the encircled region as indicated in Fig. 9b.

Region II is located at a depth of more than 1 μm from the surface and is composed of a parallel set of deformation twins that populate the grains at microscale. The thickness of the twins is reduced closer to the surface. The high fraction of deformation twins along with high dislocation density are observed in region II (Fig. 10a). Furthermore, several features that suggest twin-twin intersections are observed at 1 μm depth below the treated surface (Figs. 10a). Two different sets of twin systems can be seen interacting together (Figs. 10b,c). High-density of dislocation loop/tangles are also observed in the interaction zone, as marked in Fig. 10c. This

observation suggests that after SMAT, the twin-twin interactions potentially facilitate the locking of the dislocation movements in this alloy. Less mobility of the dislocations in the localized regions promotes dislocation partials to get active that causes the formation of stacking faults, twins and sometimes leads to local transformations.
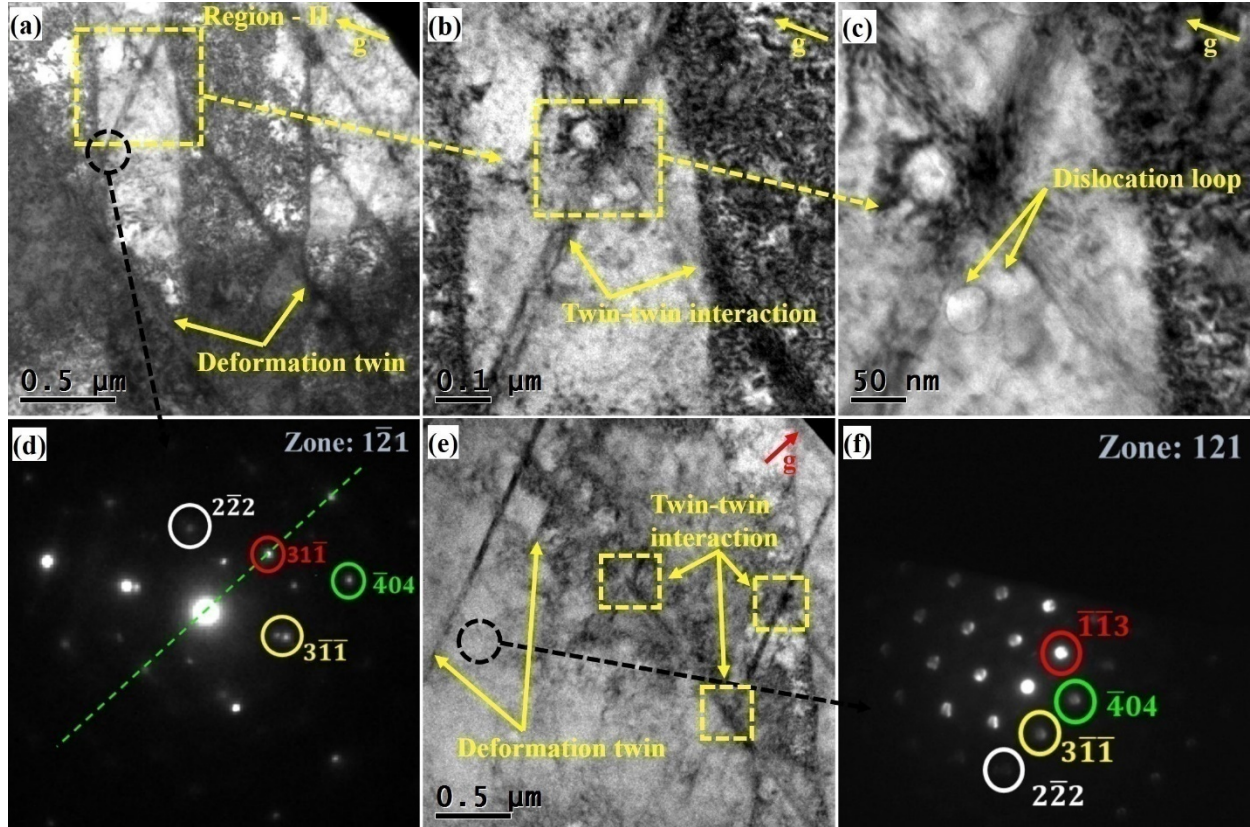

Fig. 10: (a) Bright-field TEM micrograph from the region ≈1 μm away from the top surface layer, (b) magnified view of the marked region as indicated in (a), (c) higher magnification view indicating the formation of dislocation loop at the marked region of (b), (d) SADP at the encircled region as indicated in (a), (e) Bright-field TEM micrograph of the same region as (a) for a different g-vector, and (f) SADP for the encircled region indicated in (e).

Figs. 10a and 10e present bright-field micrographs with the two different g-vectors. While the interacting deformation twins are observed along with the dislocation forest in one micrograph, these are absent in the micrograph corresponding to another g-vector. This indicates that at some locations, only partial dislocations are active that lead to the formation of twins and/or stacking faults. This phenomenon is for a long-range and concise width leading to the formation of the deformation twin with a larger length [32,33]. It is well known that partial

dislocations are responsible for the twin and stacking fault formation [32-34]. In the present case, because of the heavy dislocations, further movement of perfect dislocation is getting hindered [32-34]. The formation of the dislocation forest is seen in the bright-field transmission electron micrograph (Fig. 10a) reported for a g-vector; however, the same is absent on changing the g-vector (Fig. 10e). The distorted lattice facilitates the activity of partials dislocations [33,34]. The presence of such partials (moving and trailing) leads to the formation of twins. This explains the presence of such a high amount of deformation twins.

Taken together, the results presented here suggest that SMAT processing for a longer duration facilitates the initiation and/or interactions of deformation twins, and with further increase in the strain, twin-twin intersections occur, which may split the original matrix grains into refined blocks. In agreement with the results reported by Huang et al. [36] and Roland et al. [37], twin-twin intersections are observed at ≈ 1 µm below the treated surface. Finally, the formation of nanocrystallites from the refined blocks occurs through grain rotation or grain boundary sliding, as observed during SPD [36,37].
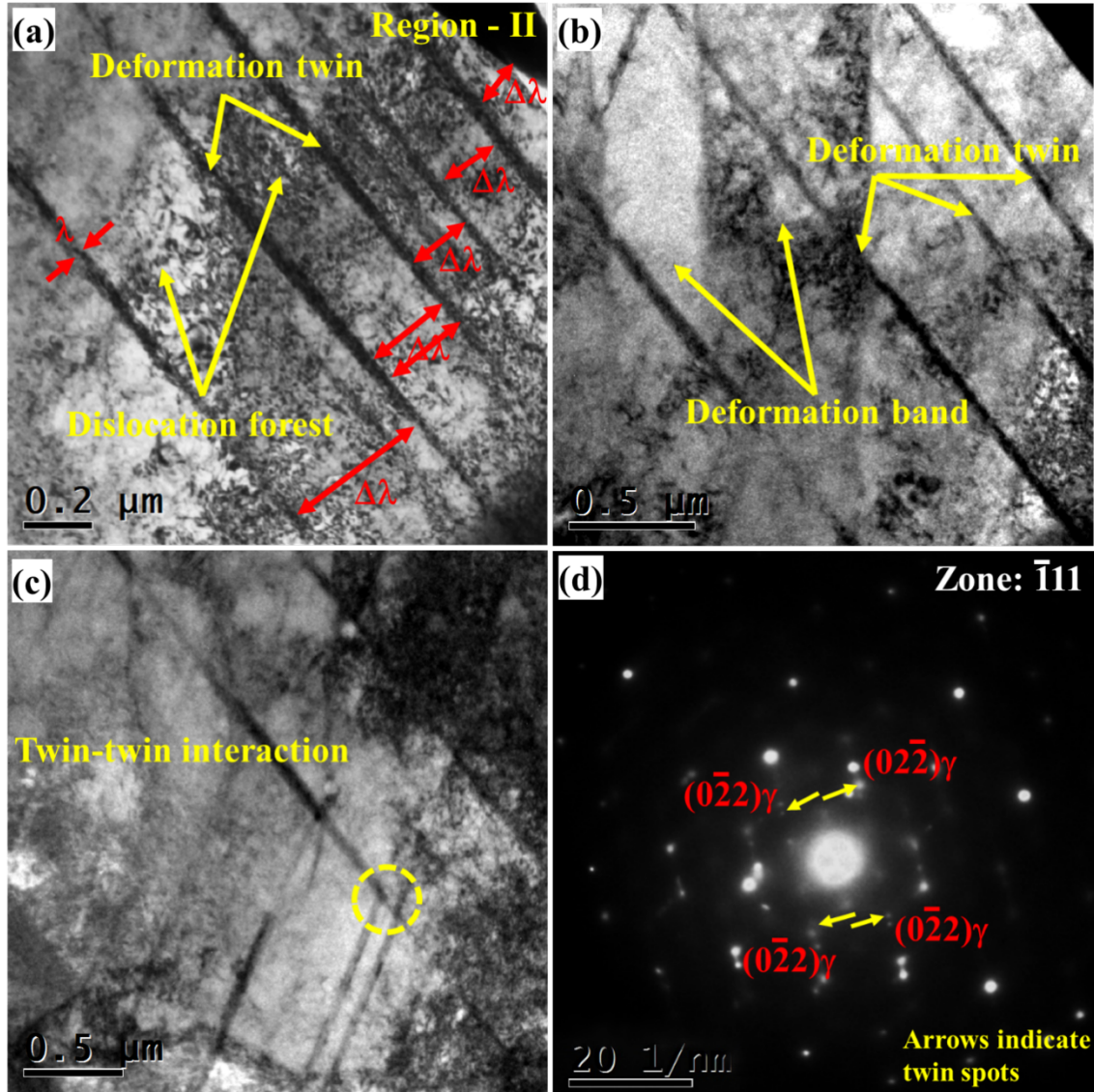
Fig. 11: Bright-field TEM micrographs showing (a) a set of parallel twins, (b) twin-deformation band interaction, (c) twin-twin interaction, (d) SADP from the encircled region as indicated in Fig. 11c.

Fig. 11a shows the formation of extremely thin deformation twins of a thickness (λ) ≈50 nm. Furthermore, it was observed that with increasing the depth, no obvious change was observed in twin thickness; however, the twin density decreases, and the distance between twins ($\Delta\lambda$) gradually increases. The variations of twin thickness and distance between twins with distance from the surface are plotted in Fig. 12. The formation of a gradient twin structure from the surface towards the bulk is seen. This is ascribed to the gradient in strain distribution due to SMAT. This also indicates that plastic deformation during the SMAT process in the present alloy

is dominated by deformation twinning mode. The topmost layer undergoes SPD, and the nanocrystalline structures are formed through twin-twin/ twin-deformation band interactions, as shown in Figs. 11b and 11c, analogous to the mechanism of formation of nanograins during the dynamic plastic deformation (DPD) process of the 316L SS [38]. Similar type of surface nanocrystalline/ nanotwinned structures form during the DPD process, and the average twin sizes are in good agreement with those in the topmost layer of the present SLM 316L SS after SMAT.
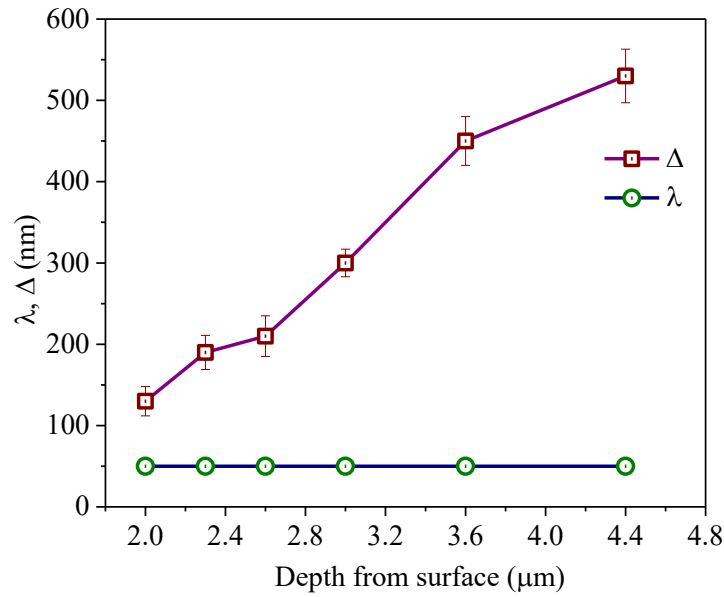

Fig. 12: Variations in twin thickness (λ) and matrix lamella thickness (Δλ) with depth.

3.4 Evaluation of mechanical properties

The gradient micro-/ nano-structure in SLM 316L SS, when subjected to SMAT, can impart changes to mechanical properties through various strengthening routes. Moreover, the thickness of the gradient layer can also play a key role in determining the mechanical properties. Hence, we studied the effect of SMAT duration on the mechanical properties of the AM alloy.

Fig. 13 presents the surface hardness profile after SMAT for 15, 30, 45, 60, or 75 min. The mean hardness steadily increased from ≈243 HV (in as-AM) to a maximum of ≈363 HV after 60 min but remained essentially unchanged at ≈359 HV after 75 min (Fig. 13).
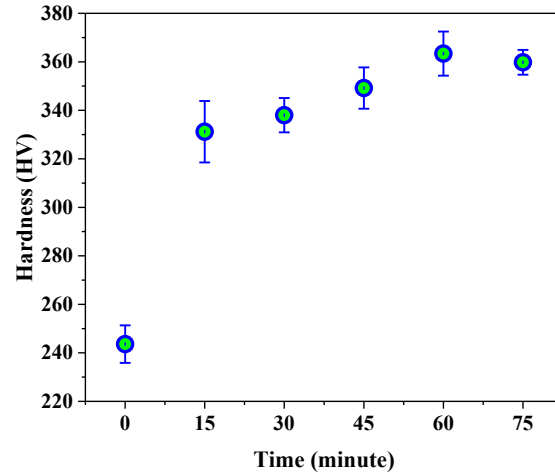
Fig. 13: Surface hardness profile of SLM 316L SS after SMAT for different durations. Data are shown as mean ± S.D. for three measurements.

Furthermore, micro-hardness measurements from surface to 500 μm depth along the cross-section at 10 μm intervals of SMAT-15 and SMAT-60 are compiled in Figs. 14a and 14b. The thickness of the treated surfaces, as measured by an increase in the hardness, was significantly affected by the duration of SMAT, corroborating the changes in microstructure described above. The hardness of the top layer was 1.3 times more than that of the unaffected bulk matrix within 15 min of SMAT and showed some additional increase after 60 min. In SMAT-15, the hardness was altered in a gradient manner up to 20 μm depth, whereas the gradient extended up to 40 μm in SMAT-60. Thus, a gradual decrease in the extent of SPD from the surface into the bulk results in a gradient of hardness associated with a gradient in grain size and other microstructural features presented above.
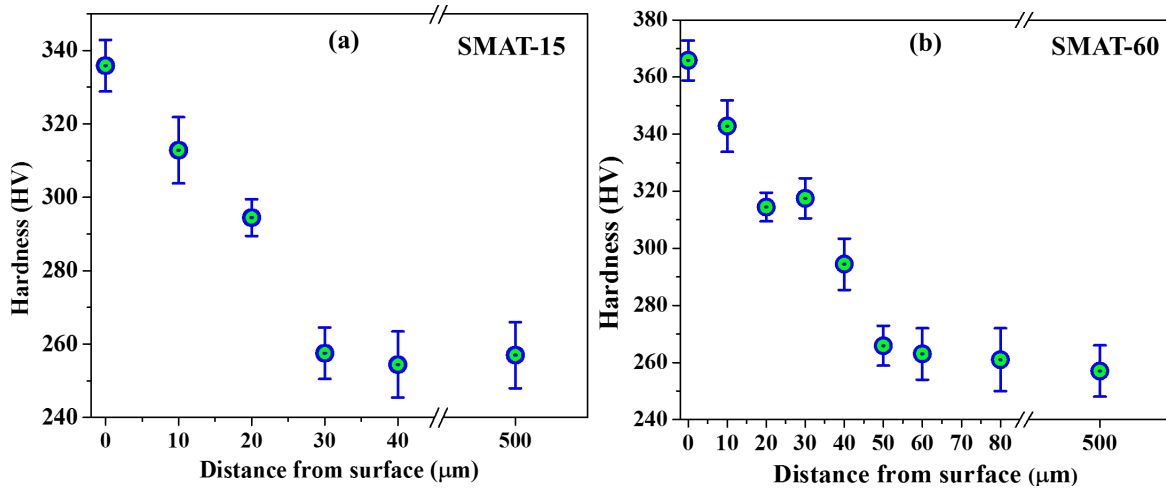
Fig. 14: Microhardness profile with the corresponding depth from the surface of (a) 15min, and (b) 60min SMAT treated specimens. Data are shown as mean ± S.D. for three measurements.

Fig. 15a shows the engineering stress *vs.* strain curves of wrought (conventionally hot rolled and annealed), as-AM, SMAT-15, and SMAT-60 SSs. As-AM exhibits much higher strength (the yield as well as tensile strengths) as compared to the wrought alloy, as has been reported earlier [30]. We attribute this to a combination of the non-equilibrium microstructure resulting from rapid cooling during additive manufacturing and the unique morphological and crystallographic textures that arise due to the layer-by-layer addition in SLM [30].

The yield strength (YS) increased from 513 ± 7 MPa of the as-AM to 569 ± 10 MPa and 603 ± 12 MPa for SMAT-15 and SMAT-60, respectively. Interestingly, the enhancement of YS could be accomplished without significant loss in ductility. SMAT-15 and SMAT-60 exhibit total elongation of 50 ± 3% and 40 ± 3%, respectively, whereas the elongation for as-AM is 59 ± 3%. The high strength is attributed to the formation of the surface nanocrystalline structure.

It is to be noted that both SMAT-15 and SMAT-60 material exhibit ultimate tensile strength (UTS) that is higher than YS, which indicates that SMAT imparts significant work-hardening ability during plastic deformation. This behavior is different from that of bulk nanostructured 316L SS produced by several different SPD [36,37] and DPD [38] processes, in which improved YS is close to UTS with a concomitant sharp decrease in the ductility. Extraordinary tensile plasticity can be achieved in nanostructured films in which strain localization is suppressed, as observed earlier [36-40].
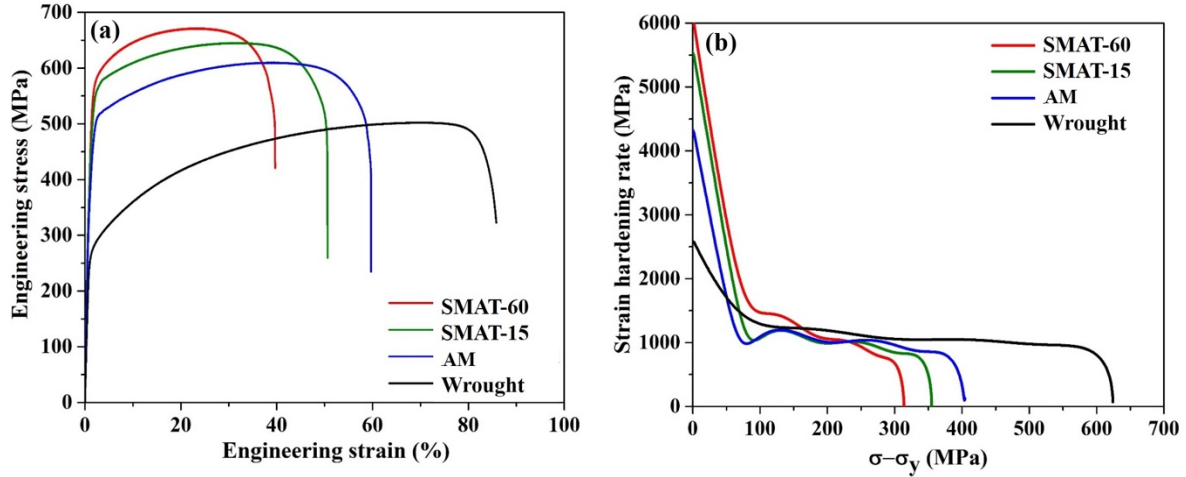
Fig. 15: (a) Engineering stress *vs.* strain curves after tensile testing of wrought and AM alloys along with the AM material subjected to SMAT, and (b) strain hardening curves of the corresponding specimens.

Fig. 15b presents the strain hardening curves of the specimens presented in Fig. 15a. In the case of AM alloys subjected to SMAT, the work hardening rate decreased as compared to the as-AM and wrought materials. SMAT-60 exhibits the lowest decrease in work hardening rate. Although the work hardening rate decreased with an increase in the duration of SMAT, it was much higher than the bulk nanostructured 316L SS [21]. This may be attributed to the gradient microstructure after SMAT such that even as the coarse grains in the matrix begin to deform plastically, the nanocrystalline surface layer may still deform elastically [39,40]. Consequently, this could lead to an increase in geometrically necessary dislocations to accommodate the large strain gradient near the migrating elastic/ plastic interfaces and later the migrating stable/ unstable interfaces [39,40].

3.5 Fractography

Figs. 16a compiles the fractographs of the as-AM alloy and after SMAT. The magnified image in Fig. 16b of the selected region of Fig. 16a indicates ductile failure associated with characteristic large-sized dimples on the fracture surface. The average dimple size is ≈5 μm. Fig. 16c shows the fractograph of SMAT-15 and Figs. 16(d-f) show the magnified micrographs of the regions marked in Fig. 16c. The fracture surface adjacent to the edges that were subjected to SMAT is remarkably different than the central location with an average dimple size of ≈1 to 2 μm. However, the central region exhibits a larger dimple size similar to those seen for as-AM. Fig. 16g shows the fractograph of SMAT-60 and Figs. 16(h-j) present the magnified micrographs of the regions marked in Fig. 16g. The average dimple size is less than 1 μm at the edges, but the

central location exhibits a larger dimple size similar to as-AM. This is ascribed to the formation of SMAT-induced gradient layer at the treated surface. The reduction in the size of dimples after SMAT is likely due to the development of the nanocrystalline grain/ nanotwinned substructure along with dislocation substructures/ cells and the associated changes in surface hardness and YS.
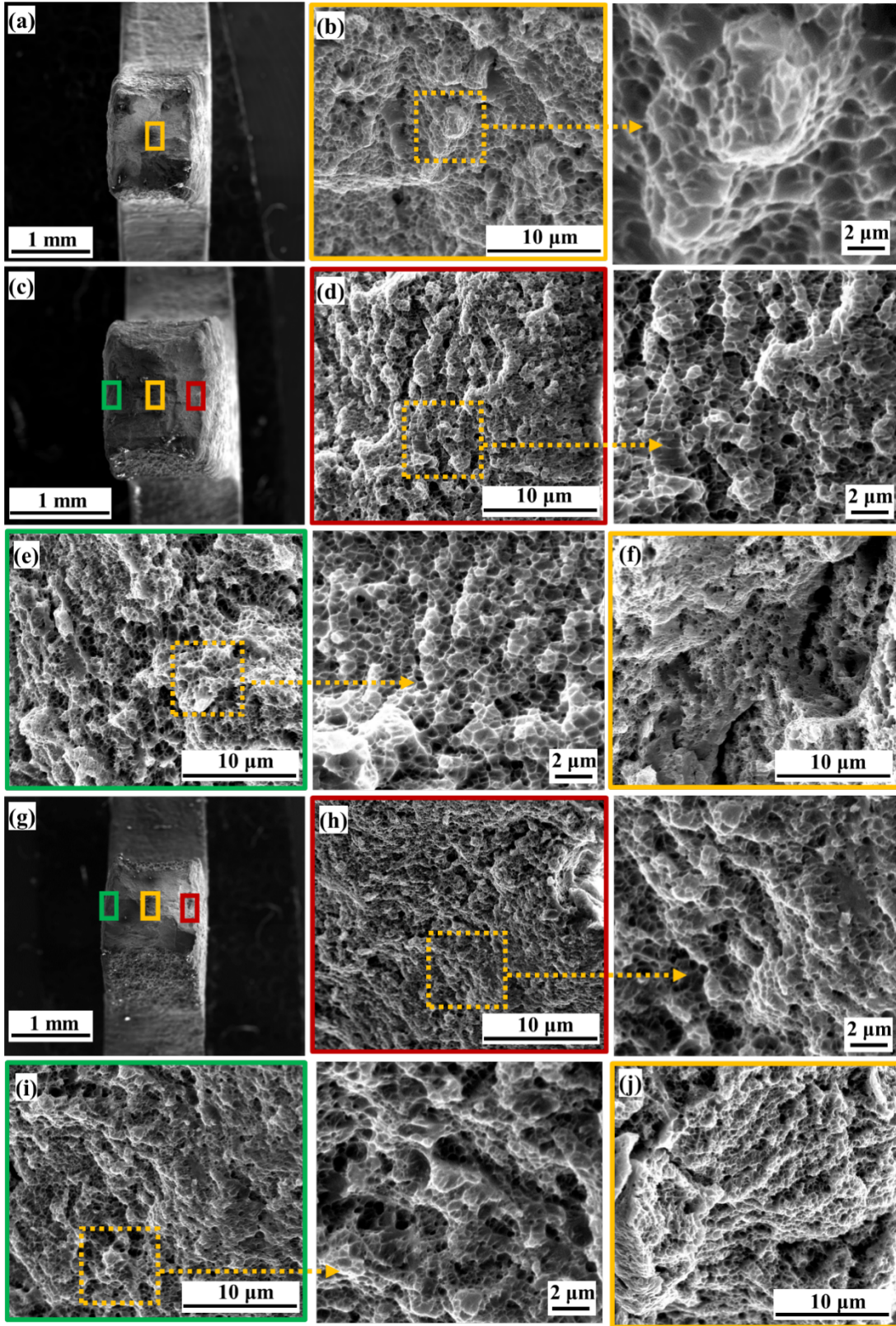
Fig. 16: Morphology of the fractured surface revealed by SEM for (a, b) additively manufactured, (c-f) SMAT-15 and (g-j) SMAT-60.

3.6 Evaluation of strengthening mechanisms

The mechanisms of grain refinement for the 316L stainless steel have been studied in detail using EBSD and TEM analyses. The information obtained from these analyses is used to gain more insights into the microstructural evolution and to determine the effectiveness of the processing parameters. Samih et al. [35] and Roland et al. [37] have reported that grain refinement is the major source of strengthening in SMAT processed 316 L SS. However, these studies did not estimate dislocation density and therefore neglected its contribution to strengthening. It is well known that dislocation density is one of the major sources of strengthening in severe plastically deformed metals in addition to grain size strengthening [21, 41]; hence the role of dislocation density on strengthening cannot be neglected. In the present study, the estimation of dislocation density and crystallite size has been carried out from the analysis of the XRD pattern using Williamson-Hall (W-H) method.

The XRD patterns of the as-AM alloy and after SMAT are displayed in Fig. 17. In austenitic SSs, the plastic deformation of the austenite phase is influenced by stacking fault energy that decides the deformation mechanism through twinning and/or martensitic transformation [19-21]. In the present study, the shift of the position of the XRD peak, as well as peak broadening, can be seen in Fig. 17 that are likely due to deformation stacking faults and residual stress in the austenite phase, respectively. Furthermore, the width of the peak steadily increases with an increase in the duration of SMAT. This is attributed to an increase in lattice strain and the decrease in the crystallite size with an increase in the duration of SMAT [21, 42, 43]. By a careful analysis of broadening of the XRD peaks, it is possible to estimate the individual contribution of lattice strain and crystallite size separately. In order to eliminate the instrumental broadening from the broadening due to lattice strain and crystallite size, a corresponding peak profile from polycrystalline Si has been used, and the contribution of lattice strain and crystallite size in the total broadening has been estimated as follows [43,44].

$$\beta_r = \sqrt{(\beta_{obs}^2 - \beta_i^2)} \qquad (1)$$

where β_r is the total broadening due to the lattice strain and crystallite size, β_i and β_{obs} are the integral breadth at the full width at half intensity maxima (FWHM) for the standard Si and SMAT treated specimens, respectively. For separating the contributions from lattice strain and

crystallite size, W-H method has been used, wherein the average peak broadening of four peaks of each specimen has been accounted for by plotting $\beta_r Cos\theta$ vs. $Sin\theta$. The observed line breadth is a sum of two terms:

$$\beta = \frac{0.9\lambda}{\tau \cos\theta} + 4\varepsilon \tan\theta \tag{2}$$

where, λ is the wavelength, θ is the Bragg angle, τ is the crystallite size, and ε is the microstrain.

The average crystallite size is given by

$$\tau = \frac{0.9\lambda}{\beta_r \cos\theta} \tag{3}$$

while the lattice strain is
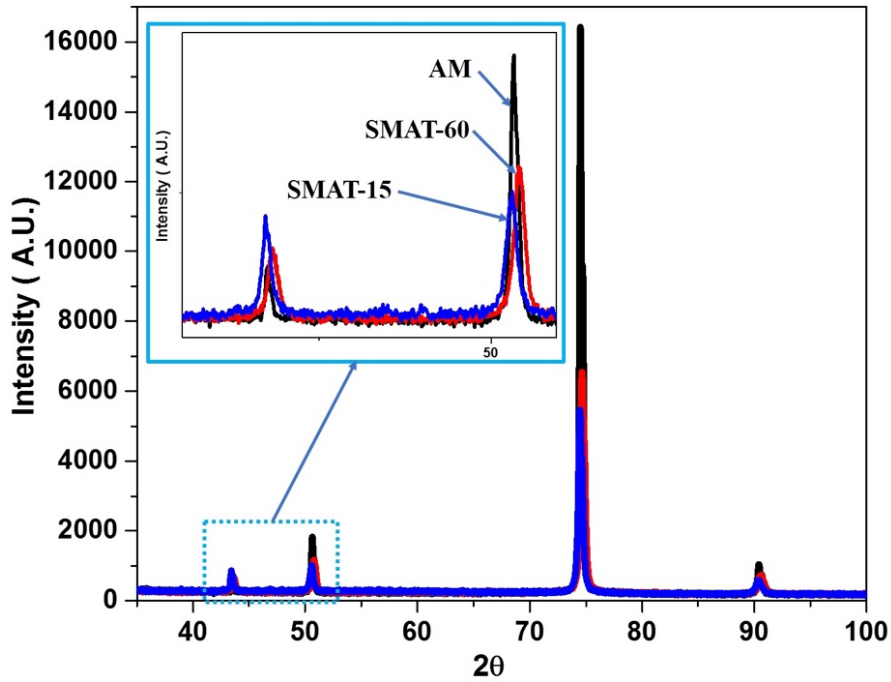
$$\varepsilon = \frac{\beta}{4\tan\theta} \tag{4}$$

Fig. 17: XRD patterns of the AM alloy before and after SMAT.

Furthermore, as described above, the enhancement in the YS after SMAT results from the combined effect of Taylor strengthening due to dislocations and grain size strengthening. We have used analytical models to estimate the individual contributions to the observed strengthening.

3.6.1 Taylor strengthening

The strengthening contribution from dislocations (σ_D) to the YS can be estimated as follows [44-46]:

$$\sigma_D = \alpha M G b \langle \rho \rangle^{1/2} \tag{5}$$

where M is the Taylor factor (3 for non-textured polycrystalline materials), G is the shear modulus (82 GPa), α is a constant and varies between 0.2 to 0.3 (in the present study α is taken as 0.3), σ_0 is the friction stress (30 MPa) and b is the Burgers vector (0.25 nm) [44-46]. 'ρ' is the dislocation density and was calculated from the XRD line profile analysis for the processed samples. The dislocation density (ρ_d) has been estimated from the following equation [45] using the average crystallite size (D) and micro-strain (ε) as follows:

$$\rho_d = \frac{2\sqrt{3}\left(\varepsilon^2\right)^{\frac{1}{2}}}{Db} \tag{6}$$

The average lattice microstrain increased from 1.3×10^{-3} to 1.7×10^{-3} with an increase in the duration of SMAT from 15 to 60 min with a concomitant decrease in the crystallite size from 92 to 79 nm. Accumulation of a large amount of lattice strain results in the formation of high-density dislocation substructures within the matrix grains [47]. The dislocation density in SMAT-15 and SMAT-60 is markedly higher than that in the as-AM alloy. The contribution of dislocations to strengthening has been calculated as 312 and 396 MPa for the SMAT-15 and SMAT-60 samples, respectively.

3.6.2 Grain size strengthening:

The contribution to YS due to grain size (σ_H) was assessed from the well-known Hall-Petch relationship as follows [43]:

$$\sigma_H = K_H d^{-1/2} \tag{7}$$

where 'd' is the grain size and K_H' is the Hall-Petch constant. 'K_H' for this alloy is reported as $\approx$ 0.11 to 0.31 MPa m$^{1/2}$ [47,48]. In this study, we have taken the value as 0.11 MPa m$^{1/2}$. Increased lattice strain and reduced grain size were observed in both SMAT-15 and SMAT-60 as compared to the as-AM alloy. The YS due to grain size was estimated to be 390, 361, and 309 MPa, respectively, for SMAT-60, SMAT-15, and as-AM, respectively, as listed in Table 1.

It is to be noted that in order to calculate the strengthening contribution due to grain size, an appropriate definition of grain is important. It is generally believed that Hall-Petch relationship is valid only with average grain size $\geq$ 1 μm and with a negligible amount of dislocations. However, it is apparent from Figs. 8 a,b that the surface of SMAT processed specimens contains nanometer-size substructures formed by dense dislocation walls. The estimated crystallite size is comparable to the average domain size, which leads to coherent X-ray diffraction leading to broadened peaks [45,46,48]. It is to be noted that X-ray diffraction is sensitive to both low angle and high-angle boundaries. At large strain deformation, many of the dislocation boundaries/low angle boundaries evolve within grains bounded by high-angle boundaries, which are indistinguishable from the original grain boundaries. Hence, it is critical to estimate the contribution of grain size and sub-grain structure in addition to dislocation substructures in SMAT processed specimens. Recently, Hasen et al. [49] demonstrated that Hall-Petch relationship derived from annealed or undeformed microstructure should be modified for extending the same to nanocrystalline materials and the microstructures that contain dislocation substructures. Therefore, based on the assumption of an identical strengthening mechanism, as reported by Hasen et al. [49], the relationship combining the Hall-Petch relationship and Taylor strengthening relationship is considered in the present study and calculated by the following equation (Eq. 8) [21, 49].

$$\sigma_{D+H} = \sigma_0 + \alpha G M b (\rho)^{1/2} + K_H d^{-1/2} \tag{8}$$

Table 1: Microstructural parameters, predicted yield strength and experimentally measured yield strength for the AM alloy in as-processed condition and after SMAT

Processing schedules	Grain size (nm)	Lattice microstrain ($\times 10^{-3}$)	Dislocation density ($\times 10^{15}\,\mathrm{m}^{-2}$)	σ_0 (MPa)	σ_H (MPa)	σ_D (MPa)	Predicted σ_y (MPa)	Experimental σ_y (MPa)
As-AM	153	1.1	1.17	25	277	246	548	513±7
SMAT-15	92	1.3	1.89	25	362	312	699	569±10
SMAT-60	79	1.7	3.05	25	391	396	812	603±12

Table 1 compiles the contribution of different strengthening mechanisms to the total yield strength (YS). It can be seen from Table 1 that the predicted YS is close to the experimental YS

of As-AM material whereas, the YS in the case of SMAT-15 and SMAT-60 is higher than the experimentally obtained YS. The difference between the calculated and experimentally measured YS values is attributed to the presence of gradient structure in SMAT specimens. In order to calculate the effect of gradient layers on the overall mechanical response, a composite strengthening model was applied. The rule of the mixture was used to compute the effect of SMAT affected zone on the overall mechanical response as follows:

$$\sigma_y = \sum v_{SMAT} \times \sigma_{SMAT} + (1 - v_{SMAT}) \times \sigma_{AM} \tag{9}$$

where v_{SMAT} is the volume fraction of the SMAT affected area, σ_{SMAT} is the yield strength of SMAT processed sample at 0.2% plastic strain, and σ_{AM} is the yield strength of the as-AM alloy. According to optical micrographs and microhardness test results (as shown in Figs. 3a,b, and 14a,b), SMAT-affected regions for 15 min and 60 min SMAT conditions are 20 and 40 μm deep, respectively. Therefore, after carrying out SMAT on both sides, the total SMAT affected area has been estimated as 40 μm (~0.05 mm) and 80 μm (~0.1 mm) respectively, for 15 min and 60 min SMAT samples. This means that the sample having an initial thickness of 1 mm has a volume fraction of SMAT affected area as 0.1% and unaffected or coarse grain volume fraction is 0.9% for 60 min SMAT condition. Considering these combinations, the estimated overall YS is presented in Table 2.

Table 2: Calculated values of YS (σ_y) using Eq. 9

Processing Schedules	Experimental σ_y (MPa) (Mean ± S.D.)	Composite strengthening model predicted σ_y (MPa)
As-AM	513 ± 7	-
SMAT-15	569 ± 10	556
SMAT-60	603 ± 12	574

It can be seen that the overall YS predicted is closer to the experimentally obtained value. Moreover, Moering [50] reported that yield stress is proportional to the hardness in each layer of gradient structure, as illustrated in Eqs. 10 and 11. In the present study, the composite strengthening model has been applied as follows:

$$\sigma_y = KHv \tag{10}$$

where K is a constant, H is the micro-hardness, and v is the volume fraction of the hardened layer. Thus, the proportion of YS of gradient layer to initial structure can be calculated as follows:

$$\sigma_{SMAT}/\sigma_{AM} = K\{v_{SMAT} \times H_{SMAT} + (1 - v_{SMAT}) \times H_{AM}\}/KH_{AM} \qquad (11)$$

Table 3: Estimated yield strength (σ_y)

Processing Schedules	Experimental σ_y (MPa)	Calculated σ_y (MPa)
As-AM	513±7	-
SMAT-15	569±10	553
SMAT-60	603±12	575

It has been found that the YS obtained from composite strengthening model based on hardness distribution is almost similar to that predicted, using Eq. 9.

3.7 Proposed mechanism of nanocrystallization due to SMAT

Based on the findings described above, the mechanism of nanocrystallization of SLM 316 SS due to SMAT is schematically presented in Fig. 18.
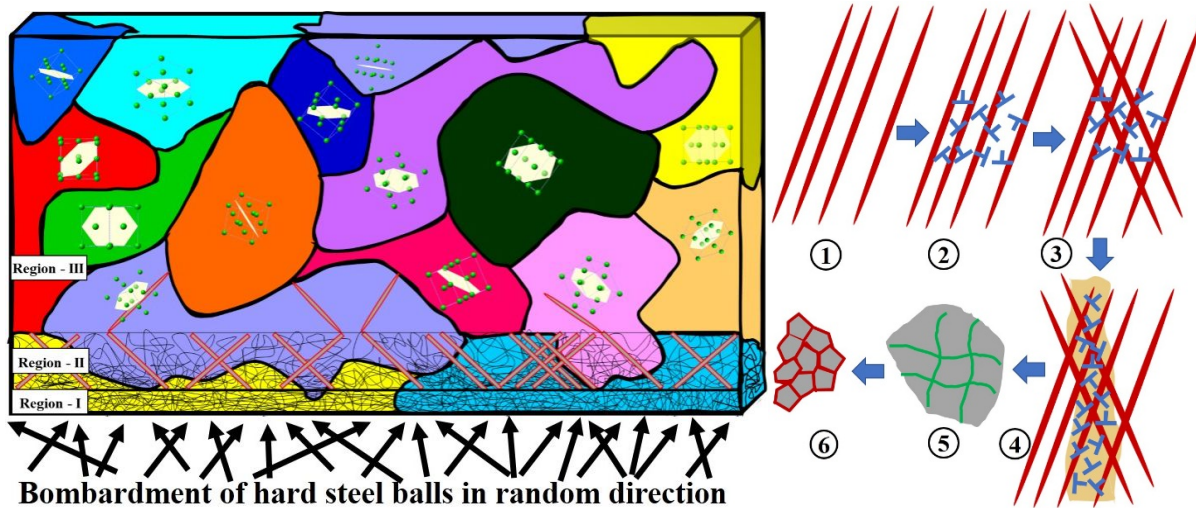

Fig. 18: Schematic description of mechanism of nanocrystallization of SLM 316 L SS due to SMAT.

A continuous bombardment of hard steel balls at a certain frequency in random directions on the surface of the alloy introduces a high density of strain-induced dislocations at the surface

and in the region in close vicinity of the surface. Very high dislocation density retards mobility of dislocations in the domain and thereby expedites the initiation of deformation twins and stacking faults. Twin density differs from one grain to another grain due to different crystallographic orientations of individual grains. A parallel set of twins in one particular direction can split the matrix grains into lamellar twin-matrix alternative blocks separated by twin boundaries. With further strain, dislocation arrays accumulate inside these twins and thereby activate another set of mechanical twins to accommodate plastic deformation. Many twins and twin-twin intersections obstruct the dislocation movements, and more dislocation loop/ tangles arise at twin boundaries across which small misorientations are induced. With further increase in the strain, the microstructure of twin/matrix lamellae can subdivide into dislocation cells or low-angle disoriented blocks, which lead to the formation of low-angle grain boundaries. The misorientation angle between subgrains gradually increases with strain through the formation of dense dislocation walls/ dislocation tangles, which acquire higher misorientations and eventually transform into subgrain boundaries. The subgrains further subdivide through a similar mechanism and finally yield grains of nanometer size.

3.8 Superior strength-ductility combination

The comparison of YS and ductility combinations for 316L SS processed by different techniques reported in the literature [51-58] and results of this work are summarized in Fig. 19. Conventional coarse-grained materials exhibit high elongation, but the strength is low. On the other hand, materials strengthened by cold rolling and SPD processes exhibit high strength, but the total elongation decreases markedly. In contrast to these techniques, the materials strengthened by nanotwin bundles by dynamic deformation-induced processes exhibit a better combination of mechanical properties. However, a superior combination of strength and ductility is observed in additively manufactured material subjected to SMAT compared to conventional micro-crystalline, bulk nanostructured, and even high-performance SS 316L. It is to be noted that the mechanical properties of the dynamic deformation-induced processed 316 L [54] subjected to appropriate annealing treatment could also provide a good combination of strength and ductility, as observed in the present work. However, the results of the present investigation clearly demonstrate the potential of SMAT as a post-processing treatment of additively manufactured

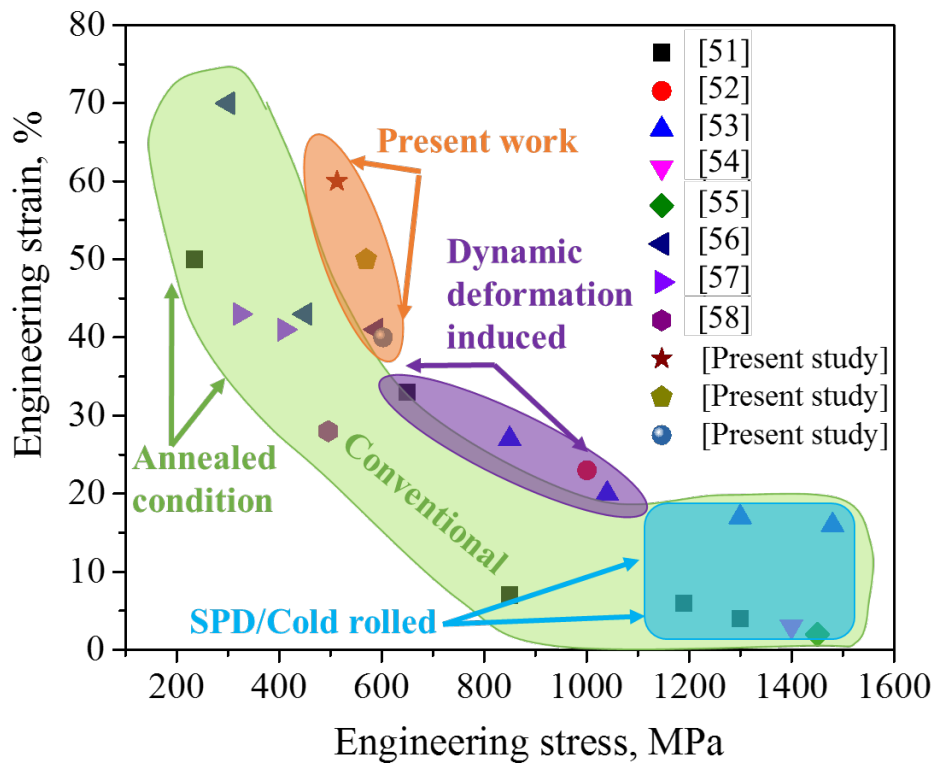316L materials to enhance yield strength retaining a good amount of ductility of SLM manufactured product.

Fig. 19: A summary of yield strength vs. elongation for various 316L SS, including the present work and reported data

4. Conclusion

In the present work, 316L SS prepared by SLM was subjected to surface engineering by SMAT. The influence of processing time on the deformation characteristics and the mechanism of nanocrystallization was investigated and was supported by a detailed study of microstructural features and mechanical properties. Following conclusions can be drawn based on the findings of this work:

1) A nanostructured surface layer followed by a gradient microstructure is obtained in the additively manufactured alloy after SMAT. The thickness of the SMAT-affected gradient layer progressively extends from 20 μm to 40 μm in-depth when SMAT duration increases from 15 to 60 min with no further changes beyond 60 min.

2) Mechanism of surface nanocrystallization due to SMAT may be summarized into the following steps: (a) introduction of dense dislocation forests/ tangles at the surface, (b)

33

initiation of deformation twins and stacking faults, (c) formation of dislocation bands, (d) formation of dislocation array inside the twins and activation of other sets of mechanical twins, (e) intersection of a large number of twin-twin/ twin-dislocation bands that obstruct the dislocation activities and formation of more dislocations loop/ tangles that arise at twin boundaries with small misorientations, (f) subdivision of twin/matrix lamellae into dislocation cells or low-angle disoriented blocks leading to the formation of low-angle grain boundaries, and (g) the division of the subgrains further through similar mechanisms to ultimately yield nanocrystalline grains.

3) The gradient microstructure at the surface provides a unique combination of mechanical properties. This is ascribed to the formation of high dislocation density and fine grains at the surface due to SMAT.

4) Analysis of the strengthening mechanisms reveals that both grain size strengthening and dislocation strengthening are key mechanisms underlying high YS of the SMAT processed SLM 316L SS. The overall strengthening could be predicted by a composite model considering the SMAT affected layer and the rest of the material.

Taken together, SMAT offers a promising route to optimize the surface characteristics and maximize the mechanical performance of SLM 316L SS for structural applications.

Acknowledgements

References

[1]   D. Herzog, V. Seyda, E. Wycisk, C. Emmelmann, Additive manufacturing of metals, Acta Mater. 117 (2016) 371-392.
[2]   R. Casati, J. Lemke, M. Vedani, Microstructure and Fracture Behavior of 316L Austenitic Stainless Steel Produced by Selective Laser Melting, J. Mater. Sci. Tech. 32 (2016) 738-744.
[3]   J. Suryawanshi, K.G. Prashanth, U. Ramamurty, Mechanical behavior of selective laser melted 316L stainless steel, Mater. Sci. Eng. A 696 (2017) 113-121.
[4]   M.L. Montero-Sistiaga, M. Godino-Martinez, K. Boschmans, J.P. Kruth, J.V. Humbeeck, K. Vanmeensel, Microstructure evolution of 316L produced by HP-SLM (high power selective laser melting), Addit. Manuf. 23 (2018) 402-410.
[5]   Y. Samiha, B. Beausir, B. Bolle, T. Grosdidier, In-depth quantitative analysis of the microstructures produced by Surface Mechanical Attrition Treatment (SMAT), Mater. Charact. 83 (2013) 129-138.

[6]   S. Bagherifard, S. Slawik, I. Fernández-Pariente, C. Pauly, F. Mücklich, M. Guagliano, Nanoscale surface modification of AISI 316L stainless steel by severe shot peening, Mater. Des. 102 (2016) 68-77.

[7]   K. Lu, J. Lu, Nanostructured surface layer on metallic materials induced by surface mechanical attrition treatment, Mater. Sci. Eng. A, 375 (2004) 38-45.

[8]   W.Y. Tsai, J.C. Huang, Yu Jia Gao, Y.L. Chung and Guan-Rong Huang, Relationship between microstructure and properties for ultrasonic surface mechanical attrition treatment, Scr. Mater. 103 (2015) 45-48.

[9]   S Bahl, P. Shreyas, M. A. Trishul, S Suwas, K Chatterjee, Enhancing the mechanical and biological performance of a metallic biomaterial for orthopedic applications through changes in the surface oxide layer by nanocrystalline surface modification, Nanoscale, 7 (2015) 7704-7716.

[10]   S Acharya, S Suwas, K Chatterjee, Review of recent developments in surface nanocrystallization of metallic biomaterials, Nanoscale, (2021).

[11]   H.W. Zhang, Z.K. Hei, G. Liu, J. Lu, K. Lu, Formation of nanostructured surface layer on AISI 304 stainless steel by means of surface mechanical attrition treatment, Acta Mater. 51 (2003) 1871-1881.

[12]   B. Thangaraj, S. Narayanan, T. S. Nellaiappan, R. Kulandaivelu, M. Ho Lee, T. Nishimura, A Facile method to modify the characteristics and corrosion behavior of 304 stainless steel by surface nanostructuring toward biomedical applications, ACS Appl. Mater. Interfaces 7 (2015) 17731-17747.

[13]   A.A. Ahmed, M. Mhaede, M. Wollmann, L. Wagner, Effect of surface and bulk plastic deformations on the corrosion resistance and corrosion fatigue performance of AISI 316L, Surf. Coat. Technol. 259 (2014) 448-455.

[14]   R. Madhavan, R.K. Ray, S. Suwas, Micro-mechanical aspects of texture evolution in nickel and nickel–cobalt alloys: role of stacking fault energy, Phil. Mag. 96 (2016) 3177-3199.

[15]   R. Madhavan, R. Ray, S. Suwas, New insights into the development of microstructure and deformation texture in nickel-60wt.% cobalt alloy, Acta Mater. 78 (2014) 222-235.

[16]   R. Madhavan, R. Ray, S. Suwas, Texture transition in cold-rolled nickel-40wt.% cobalt alloy, Acta Mater. 74 (2014) 151-164.

[17]   G.T. Gray, Deformation twinning in Al-4.8 wt% Mg, Acta Mater. 36 (1988) 1745-1754.

[18]   K. Lu, J. Lu, Surface nanocrystallization (SNC) of metallic materials-presentation of the concept behind a new approach, J. Mater. Sci. Technol. 15 (1999) 193-197.

[19]   S.W. Hwang, J.H. Ji, K.-T. Park, Effects of Al addition on high strain rate deformation of fully austenitic high Mn steels, Mater. Sci. Eng. A 528 (2011) 7267-7275.

[20]   J. Talonen, H. H€anninen, Formation of shear bands and strain-induced martensite during plastic deformation of metastable austenitic stainless steels, Acta Mater. 55 (2007) 6108-6118.

[21]   S. Bahl, S. Suwas, T. Ungar, K. Chatterjee, Elucidating microstructural evolution and strengthening mechanisms in nanocrystalline surface induced by surface mechanical attrition treatment of stainless steel, Acta Mater. 122 (2017) 138-151.

[22]   R. Ueji, N. Tsuchida, D. Terada, N. Tsuji, Y. Tanaka, A. Takemura, K. Kunishige, Tensile properties and twinning behavior of high manganese austenitic steel with fine-grained structure, Scr. Mater. 59 (2008) 963-966.

[23]   M.S. Tsai, C.P. Chang, Grain size effect on deformation twinning in Mg–Al–Zn alloy, Mater. Sci. Technol. 29 (2013) 759-763.

[24]   P. Yang, Q. Xie, L. Meng, H. Ding and Z. Tang, Dependence of deformation twinning on grain orientation in a high manganese steel, Scr. Mater. 55 (2006) 629-631.

[25]   L. Meng, P. Yang, Q. Xie, H. Ding and Z. Tang, Dependence of deformation twinning on grain orientation in compressed high manganese steels, Scr. Mater. 56 (2007) 931-934.

[26]   Y.T. Zhu, X.Z. Liao, X.L. Wu, Deformation twinning in nanocrystalline materials, Prog. Mater. Sci. 57 (2012) 1-62.

[27] Y.T Zhu, X.Z. Liao, X.L Wu, J. Narayan, Grain size effect on deformation twinning and detwinning. J. Mater. Sci. 48 (2013) 4467-4475.

[28] L. Liu, Q. Ding, Y. Zhong, J. Zou, J. Wu, Y-L. Chiu, J. Li, Z. Zhang, Q. Yu, Z. Shen, Dislocation network in additive manufactured steel breaks strength–ductility trade-off, Mater. Today 21 (2018) 354-361.

[29] S. Acharya, A.G. Panicker, V. Gopal, S.S. Dabas, G. Manivasagam, S. Suwas, K. Chatterjee, Surface mechanical attrition treatment of low modulus Ti-Nb-Ta-O alloy for orthopedic applications, Mater. Sci. Eng. C 110 (2020) 110729.

[30] S. Bahl, S. Mishra, K.U. Yazar, I.R. Kola, K. Chatterjee, S. Suwas, Non-equilibrium microstructure, crystallographic texture and morphological texture synergistically result in unusual mechanical properties of 3D printed 316L stainless steel, Addit. Manuf. 28 (2019) 65-77.

[31] Ruslan Valiev, Nanostructuring of metals by severe plastic deformation for advanced properties, Nat. Mater. 3 (2004) 511-516.

[32] F. Zhang, X. Feng, Z. Yang, Dislocation-Twin Boundary Interactions Induced Nanocrystalline via SPD Processing in Bulk Metals, Sci. Report 5, (2015) 8981.

[33] J. Wang, H. Huanga, Shockley partial dislocations to twin: Another formation mechanism and generic driving force, Appl. Phys. Lett. 85 (2004) 5983-5985.

[34] R.E. Smallman, A.H.W. Ngan, Modern Physical Metallurgy, 8th ed., 2014, 121-158.

[35] Y. Samih, B. Beausir, B. Bolle, T. Grosdidier, In-depth quantitative analysis of the microstructures produced by Surface Mechanical Attrition Treatment (SMAT), Mater. Charact. 83 (2013) 129-138.

[36] H.W. Huang, Z.B. Wang, J. Lu and K. Lu, Fatigue behaviors of AISI 316L stainless steel with a gradient nanostructured surface layer, Acta Mater. 87 (2015) 150-160.

[37] T. Roland, D. Retraint, K. Lu, J. Lu, Fatigue life improvement through surface nanostructuring of stainless steel by means of surface mechanical attrition treatment, Scr. Mater. 54 (2006) 1949-1954.

[38] H.T. Wang, N.R. Tao, K. Lu, Strengthening an austenitic Fe–Mn steel using nanotwinned austenitic grains, Acta Mater. 60 (2012) 4027-4040.

[39] X.L. Wu, P. Jiang, L. Chen, J. F. Zhang, F. P. Yuan, Y. T. Zhu, Synergetic Strengthening by Gradient Structure, Mater. Res. Let. 2 (2014) 185-191.

[40] X.L. Ma, C.X. Huang, W.Z. Xu, H. Zhou, X.L. Wu, Y.T. Zhu, Strain hardening and ductility in a course-grain/nanostructure laminate material. Scr. Mater. 103 (2015) 57-60.

[41] R. Kalsar, D. Yadav, A. Sharma, H.G. Brokmeier, J. May, H.W. Höppel, W. Skrotzki, S. Suwas, Effect of Mg content on microstructure, texture and strength of severely equal channel angular pressed aluminium-magnesium alloys, Materials Science and Engineering A, 797 (2020) 140088.

[42] A. Sarkar, A. Bhowmik, S Suwas, Microstructural characterization of ultrafine-grain interstitial-free steel by X-ray diffraction line profile analysis, Appl. Phys. A 94 (2009) 943-948.

[43] T. Ungar, S. Ott, P.G. Sanders, A. Borbely, J.R. Weertman. Dislocations, grain size and planar faults in nanostructured copper determined by high resolution X-ray diffraction and a new procedure of peak profile analysis, Acta Mater. 46 (1998) 3693-3699.

[44] W.F. Smith, J. Hashemi, Foundations of materials science and engineering, 4th ed. McGraw-Hill, (2006) 242-243.

[45] Z. Wang, W. Luan, J. Huang, C. Jiang, XRD investigation of microstructure strengthening mechanism of shot peening on laser hardened 17-4PH, Mater. Sci Eng A 528 (2011) 6417-6425.

[46] F. HajyAkbary, J. Sietsma, A.J. Böttger, M.J. Santofimia, An improved X-ray diffraction analysis method to characterize dis- location density in lath martensitic structures, Mater. Sci. Eng. A 639 (2015) 208-218.

[47] K. Takeda, N. Nakada, T. Tsuchiyama, S. Takaki, Effect of Interstitial Elements on Hall-Petch Coefficient of Ferritic Iron, ISIJ Int. 48 (2008) 1122-1125.

[48]   A. Shibata, T. Nagoshi, M. Sone, S. Morito, Y. Higo, Evaluation of the block boundary and sub-block boundary strengths of ferrous lath martensite using a micro-bending test, Mater. Sci. Eng. A 527 (2010) 7538-7544.

[49]   N. Hansen, Hall-Petch relation and boundary strengthening, Scr. Mater. 51 (2004) 801-806.

[50]   J. Moering, X. Ma, J. Malkin, M. Yang, Y. Zhu, S. Mathaudhu, Synergetic strengthening far beyond rule of mixtures in gradient structured aluminum rod, Scr. Mater. 122 (2016) 106-109.

[51]   B.R. Kumar, S. Sharma, B. Mahato, Formation of ultrafine grained microstructure in the austenitic stainless steel and its impact on tensile properties, Mater. Sci. Eng. A 528 (2011) 2209-2216.

[52]   G.Z. Liu, N.R. Tao, K. Lu, 316L austenite stainless steels strengthened by means of nano-scale twins, J. Mater. Sci. Technol. 26 (2010) 289-292.

[53]   H. Ueno, K. Kakihata, Y. Kaneko, S. Hashimoto, A. Vinogradov, Enhanced fatigue properties of nanostructured austenitic SUS 316L stainless steel, Acta Mater. 59 (2011) 7060-7069.

[54]   F.K. Yan, G.Z. Liu, N.R. Tao, K. Lu, Strength and ductility of 316L austenitic stainless steel strengthened by nano-scale twin bundles, Acta Mater. 60 (2012) 1059-1071.

[55]   X.H. Chen, J. Lu, L. Lu, K. Lu, Tensile properties of a nanocrystalline 316L austenitic stainless steel, Scr. Mater. 52 (2005) 1039-1044.

[56]   K. Lu, F. K. Yan, H.T. Wang, N.R. Tao, Strengthening austenitic steels by using nanotwinned austenitic grains, Scr. Mater. 66 (2012) 878-883.

[57]   W. Zielinski, A.A. Abduluyahed, K.J. Kurzydowski, TEM studies of dislocation substructure in 316 austenitic stainless steel strained after annealing in various environments, Mater. Sci. Eng. A 249 (1998) 91-96.

[58]   T.M. Mower, M.J. Long, Mechanical behavior of additive manufactured, powder-bed laser-fused materials, Mater. Sci. Eng. A 651, (2016) 198-213.